JARO 16: 101–119 (2015)
DOI: 10.1007/s10162-014-0494-4

JARO
Journal of the Association for Research in Otolaryngology

Research Article

Reverse Correlation Analysis of Auditory-Nerve Fiber Responses to Broadband Noise in a Bird, the Barn Owl

Bertrand Fontaine,[1,2] Christine Köppl,[3] and Jose L Peña[1]

[1]*Dominick P. Department of Neuroscience, Albert Einstein College of Medicine, Bronx, NY 10461, USA*

[2]*Laboratory of Auditory Neurophysiology, University of Leuven, 3000, Leuven, Belgium*

[3]*Cluster of Excellence "Hearing4all" and Research Center Neurosensory Science and Department of Neuroscience, School of Medicine and Health Science, Carl von Ossietzky University, 2612, Oldenburg, Germany*

Received: 23 April 2014; Accepted: 24 September 2014; Online publication: 15 October 2014

ABSTRACT

While the barn owl has been extensively used as a model for sound localization and temporal coding, less is known about the mechanisms at its sensory organ, the basilar papilla (homologous to the mammalian cochlea). In this paper, we characterize, for the first time in the avian system, the auditory nerve fiber responses to broadband noise using reverse correlation. We use the derived impulse responses to study the processing of sounds in the cochlea of the barn owl. We characterize the frequency tuning, phase, instantaneous frequency, and relationship to input level of impulse responses. We show that, even features as complex as the phase dependence on input level, can still be consistent with simple linear filtering. Where possible, we compare our results with mammalian data. We identify salient differences between the barn owl and mammals, e.g., a much smaller frequency glide slope and a bimodal impulse response for the barn owl, and discuss what they might indicate about cochlear mechanics. While important for research on the avian auditory system, the results from this paper also allow us to examine hypotheses put forward for the mammalian cochlea.

Correspondence to: Bertrand Fontaine · Laboratory of Auditory Neurophysiology · University of Leuven · 3000, Leuven, Belgium. Telephone: +32 16 37 29 38; email: bertrand.fontaine@med.kuleuven.be

Keywords: reverse correlation, spike-triggered average, cochlear mechanics

INTRODUCTION

The barn owl is a well-established species in auditory research because of its superior ability to acoustically localize prey. While the neural circuits involved in the formation of a map of space in the central auditory system have been well characterized, less attention has been paid to the sensory organ, the basilar papilla. The avian basilar papilla shares a common origin with (i.e., is homologous to) the mammalian cochlea but has evolved salient specializations independently from its mammalian counterpart (Manley and Köppl 1998; Köppl 2011) to achieve equivalent functions. Surprisingly, clear morphological differences can still result in auditory nerve responses with similar characteristics such as group delays and frequency tuning (Köppl 1997b; Ruggero and Temchin 2007). While fundamental for research on the auditory system of birds, a better understanding of the avian cochlea can also help gain insight into the mammalian cochlea, by comparing similarities and differences in morphology and physiology.

Direct mechanical measurements at basal sites of the mammalian cochlea are available (de Boer and Nuttall 1997; Recio et al. 1998; Recio-Spinoso et al. 2009). These invasive techniques are potentially very harmful for the vulnerable cochlea. Therefore, re-

sponses at the auditory nerve continue to serve as an access point to cochlear mechanisms (van der Heijden and Joris 2003; Recio-Spinoso et al. 2005; Temchin et al. 2011; Versteegh et al. 2011). Barn owl auditory nerve responses have been studied with tones (Köppl 1997a, b). However, the highly nonlinear character of auditory transduction restricts the characterization of cochlear mechanics using pure-tone stimulation. Experiments presenting broadband stimuli have been extensively performed in the mammalian auditory system (e.g., de Boer and de Jongh 1978; Carney and Yin 1988; van der Heijden and Joris 2003; Recio-Spinoso et al. 2005; Versteegh et al. 2011) as they are thought to linearize the system for a fixed input level (Recio-Spinoso et al. 2009).

In this paper, for the first time in any avian species, we studied the impulse responses of auditory-nerve fibers (ANF) of barn owls, derived from reverse correlation of broadband noise responses. Using linear filters, we studied the relationship between properties of the transfer functions like phase modulation, sharpness of frequency tuning, and response delays, which can be informative about the underlying cochlear mechanisms (Tan and Carney 2003; van der Heijden and Joris 2003; Recio-Spinoso et al. 2005; Temchin et al. 2011; Versteegh et al. 2011). Where possible, we compared the owl's AN transfer function features to published data in mammals. This comparison rests on the assumption that our data closely reflect the mechanical input to the hair cells. A potential confounding factor is the well-known phenomenon of electrical tuning by hair-cell membrane channel properties which undoubtedly plays a role in avian hair cells. However, its direct demonstration remains limited to frequencies below 1 kHz (Fuchs et al. 1988; Tan et al. 2013), and its contribution is likely to diminish with increasing frequency. While the upper frequency limit is not precisely known, model estimates using realistic assumptions placed it at around 5 kHz. This is consistent with the highest characteristic frequencies where preferred intervals in the spontaneous discharge of auditory-nerve fibers (an indirect indication of electrical tuning) have been observed in the barn owl (Köppl 1997a). As the bulk of our recordings were from fibers with characteristic frequencies (CFs) above 5 kHz, any contribution of electrical tuning is likely to be minimal. We thus assume that the reverse correlations closely reflect the mechanical input to the tall hair cells which in turn provide the input to afferent nerve fibers. We show qualitative agreement with mammalian data to a large extent, but also some intriguing quantitative differences, e.g., a much smaller frequency glide slope and a bimodal impulse response for the barn owl. The implications of these differences and similarities for the underlying cochlear mechanics are discussed.

MATERIALS AND METHODS

Experiments were performed on six adult barn owls, in two different laboratories (five owls in one laboratory, and one owl in the other) but using largely identical procedures. The procedures complied with guidelines set forth by the National Institutes of Health and were approved by the Albert Einstein College of Medicine's Institute of Animal Studies, and the Animal Ethics Committee of Lower Saxony, Germany, respectively.

Anesthesia and Surgery

General anesthesia was induced and maintained by intramuscular injections of ketamine hydrochloride (5–20 mg/kg) and xylazine (2–4 mg/kg). Maintenance of body temperature was either assisted by a heating pad wrapped around the body of the owl (American Medical Systems, Minnesota, USA) or held at 39 °C by a feedback-controlled blanket system (Harvard Instruments, Massachusetts, USA). Animals breathed unaided; however, one owl was intubated through a tracheotomy to avoid potential problems with salivation. A metal piece was fixed to the skull with dental cement, to hold the head firmly. The bone and meninges overlying the right cerebellum were removed, and the posterior part of the right cerebellum was aspirated to expose the surface of the auditory brainstem on that side.

Acoustic Stimulation and Calibration

All recordings were performed in a double-walled sound-attenuating chamber (Industrial Acoustics Corporation, Winchester, UK, and Bronx, USA). Closed sound systems were inserted into both ear canals and consisted of a miniature speaker (Knowles 1914, Knowles Electronics, Illinois, USA or Aiwa HP-V14, Tokyo, Japan) and a microphone (Knowles 1319 or Knowles FG 23329) each, contained in a custom-made housing that fit the owl's ear canal. Previous calibration of the Knowles microphones with a Brüel and Kjaer (Naerum, Denmark, Model 4190 or 4134) microphone made it possible to translate the voltage output of the Knowles into sound level in dB SPL. The Knowles microphones were used to calibrate the earphone assemblies at the beginning of each experiment. The calibration data contained the amplitudes and phase angles measured in frequency steps of 100 Hz. The stimulus-generation software then used these calibration data to automatically correct irregularities in the amplitude and phase response of each earphone between 0.5 and 12 kHz.

Tonal stimuli and Gaussian white noises filtered between 0.5 and 10 or 12 kHz were synthesized by

custom-written software and a signal processing board (AP2, Tucker-Davis Technologies). Stimuli were gated with 5 ms rise/fall times. Manual attenuators were used to adjust the overall sound levels in both ears; software-controlled attenuators (PA4, Tucker-Davis Technologies) varied the stimulus levels during data collection.

Electrophysiology

Glass microelectrodes, filled with either 2 M K-acetate or 3 M KCl and with impedances mostly between 30 and 60 MΩ, were positioned under visual control above the surface of the brainstem and then advanced under remote control. Neural signals were serially amplified by a Multiclamp 700B (Molecular Devices, Sunnyvale, California) or a WPI 767 (World Precision Instruments, Sunnyvale, California) and an AC amplifier (PC1, Tucker-Davis Technologies). A spike discriminator (SD1, Tucker-Davis Technologies, Alachua, Florida) converted neural impulses into transistor–transistor logic pulses for an event timer (ET1, Tucker-Davis Technologies), which recorded the timing of the pulses. In parallel, the analog waveforms were stored in a personal computer via an analog-to-digital converter (DD1, Tucker Davis Technologies) with a sampling rate of 48 kHz and 16-bit resolution. A computer was used for preliminary online data analysis and display.

Data Collection Protocol

Since quantitative data were only collected for auditory-nerve units, all stimulation protocols were exclusively ipsilateral. After isolating a unit, some basic tests were run, using stimuli of 50 ms duration, 5 ms rise/fall times, presented at a rate of 5/s: CF was estimated audiovisually, by reducing the stimulus level until the response could only be discerned within approximately ±200 Hz. Next, a rate-level curve for noise stimuli was recorded, in 5 dB steps, repeated 10 or 20 times. This was used to guide the choice of levels for subsequent noise presentations.

Data for reverse correlation were obtained by presenting 200-ms de novo-synthesized broadband signals. Stimuli were presented with an inter-stimulus interval of 500 ms (commonly prolonged by the high processing demands of continuously synthesizing the stimuli de novo), and we attempted to collect at least 2,000 spikes for each stimulus condition. In most cases, responses to three sound levels, within a range from near threshold to saturation levels, were recorded in one collective run, with levels being randomly presented. The noise levels given are overall levels.

Spike Triggered Average Computation and Fitting

The impulse response was calculated from the spike triggered average (STA). For a broadband noise stimulus, the impulse response $h(t)$ is the average stimulus that elicits spikes (de Boer and de Jongh 1978; Schwartz et al. 2006), that is, $h(t) = \frac{1}{N}\sum_{n=1}^{N} \vec{s}(t_n)$, where t_n is the time of the n_{th} spike, $\vec{s}(t_n)$ is a vector containing the stimulus present in a temporal window preceding that spike and N is the total number of spikes in the analysis. Based on visual inspection of the STAs, we set the analysis window to be 15 ms, i.e., we considered that impulse responses are shorter than 15 ms.

We fitted the resulting STAs to analytical functions called gammachirps (Wagner et al. 2009; Fischer et al. 2011; Fontaine et al. 2013, 2014). The functions consisted in the product of a high-frequency chirp with a gamma envelope. We first considered two types of chirps. The first one was based on measurements reported in the auditory nerve of cats. Its instantaneous frequency increases linearly with time (Carney et al. 1999; Fischer et al. 2011); we refer to it as the linear gammachirp GC_{lin}:

$$GC_{lin}(t) = A\,(t-t_0)^n \exp\left(-\frac{t-t_0}{\tau}\right) \cos\left(2\pi\left[f_0(t-t_0) + 0.5c(t-t_0)^2\right] + \theta\right) H(t-t_0) \quad (1)$$

where A is a scaling factor, t_0 is a pure delay, τ defines the temporal width of the gamma envelope, f_0 is the starting frequency of the carrier, θ is a phase shift, and $H(t)$ is the Heaviside function. n is the order of the gamma function and sets the degree of symmetry of the envelope (the envelope converges to a Gaussian as n increases).

In the second type of chirp, proposed by Irino and Patterson (2001), the instantaneous frequency saturates when t grows to infinity. We refer to it as the logarithmic gammachirp $GC_{\log}$ (Wagner et al. 2009):

$$GC_{log}(t) = A\,(t-t_0)^n \exp\left(-\frac{t-t_0}{\tau}\right) \cos\left(2\pi\left[f_0(t-t_0) + c\,log(t-t_0)\right] + \theta\right) H(t-t_0) \quad (2)$$

In both GC_{lin} and $GC_{\log}$, the parameter c characterizes the rate of the chirp. As the instantaneous frequency f_{inst} is defined as the temporal derivative of the phase, $f_{\text{inst}}=f_0+ct$ for GC_{lin} and $f_{\text{inst}}=f_0+c/t$ for $GC_{\log}$. Thus, f_0 can be seen as the starting frequency of the chirp in the linear case, and as the frequency to which the carrier converges as t grows in the logarithmic case.

Superposition of two of the gamma chirps were used when the STA envelope was not well fitted by a simple gamma function:

$$GC_{\text{double}}(t) = GC_1(t) + GC_2(t) \tag{3}$$

with $GC_1(t)$ and $GC_2(t)$ being either linear or logarithmic gamma chirp with independent parameters.

These functions, simple or double gamma chirps, were fitted to the STA in order to minimize the error $\chi^2 = \frac{1}{N-M}\sum_{i=1}^{N}\frac{(h(t_i)-g(t_i))^2}{\sigma_i^2}$, where $g(t)$ refers to either $GC_{\text{lin}}(t)$, $GC_{\log}(t)$, or $GC_{\text{double}}(t)$. N is the number of time points where the envelope of the STA is above the noise floor (given by the variance of the STAs far away from t=0), M is the number of parameters to fit, and σi^2 is an estimate of the variance of the STA at time point t_i across all presented trials. The optimization was implemented with an evolution algorithm (Rossant et al. 2013).

Instantaneous Frequency

The instantaneous frequency (IF) of a narrow-banded signal $x(t)$ can be conceptualized as the frequency of a sine wave that locally fits the oscillatory characteristic of that signal (Kijewski-Correa and Kareem 2006). IF is defined as the derivative with respect to time of the instantaneous phase:

$$IF(t) = \frac{1}{2\pi}\frac{d\theta(t)}{dt} \tag{4}$$

The phase is retrieved from the analytical signal $z(t)=x(t)+iH[x(t)]$: $\theta(t)=\angle z(t)$. $H[x(t)]$ is the Hilbert transform of $x(t)$:

$$H[x(t)] = \frac{1}{\pi}P\int_{-\infty}^{+\infty}\frac{x(s)}{t-s}ds \tag{5}$$

where P denotes the Cauchy principal value. Because computing IF via Hilbert transform is very sensitive to noise, we applied the calculation on the noiseless STA fits. Note that the envelope of the signal is the magnitude of the analytic signal.

Statistics and Sensitivity Measurements

Statistics are given in mean±standard deviation. All statistics were computed using Scipy, an open source scientific tools for Python (http://www.scipy.org/). To test whether parameters were correlated with best frequency (BF), we made linear regressions from which statistics were computed. When not specified, this regression was made using the responses with levels smaller than 25 dB. The slopes and intercepts of the regression lines and their corresponding statistics were computed using the Scipy function *linregress*. The resulting lines were given as Y=slope*X+intercept where X is the regressor (BF in this case) and Y the regressant. The units of both slope and intercept are given. R^2 corresponds to the square of the correlation coefficient, and p is a two-sided $p$value for a hypothesis test whose null hypothesis is that the slope is 0. The results are given as (R^2, p, and regression line). The sensitivity of a given feature against input levels was the slope of the regression with the input level, in decibels, as the regressor and the corresponding feature value as the regressant.

RESULTS

Spike recordings of auditory nerve fibers (n=116) from six barn owls were used in the present study. The distribution of CFs in our sample is heavily skewed towards high frequencies and approximately reflects the relative numbers of fibers innervating the different regions of the barn owl basilar papilla (Köppl 1997c). Each cell was presented with at least three input levels spanning most of its dynamic range: one level around 10 dB above threshold (computed with noise rate curve), one around the middle of the dynamic range, and one around saturation. A subset of cells were presented with four (n=8) and five (n=4) input levels. Stimuli consisted of broadband noise generated de novo at each presentation allowing the computation of a spike triggered average for each level. The number of presentations was chosen to yield at least 2,000 spikes per level.

Conventional reverse correlation techniques require neurons to phase lock to the stimulus fine structure (de Boer and de Jongh 1978). While they can be used across the whole hearing range of the barn owl where phase locking is present (Köppl 1997b), for mammals, such techniques are limited to the phase locking range. Some authors circumvented this limitation by designing new techniques that rely on the non-linear properties of the cochlea (Lewis et al. 2002; van der Heijden and Joris 2003; Recio-Spinoso et al. 2005). This allowed us to compare our data with recordings in mammals in not only the low but also the high-frequency range.

Impulse Response Analysis

Examples of STAs are shown in Figure 1A (i) and in grey in Figure 1B, and C, as well as in Figure 2A. We define the BF of a neuron at a given input level as the frequency of the peak of the corresponding frequency

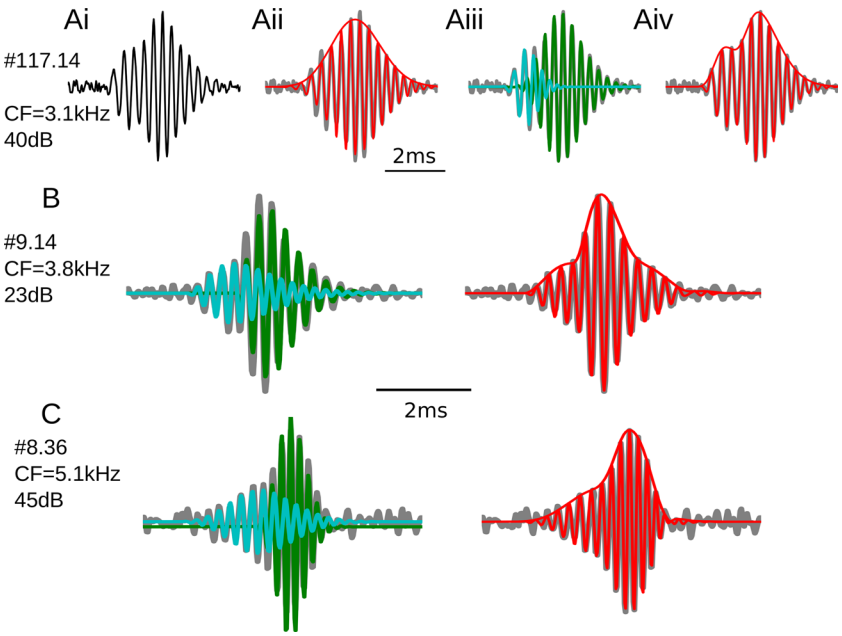

FIG. 1. Fitting analytical functions to impulse responses. **A** *i*: the reverse correlation was computed through the spike triggered average (STA). Note that the STA seems to contain two components. **A** *ii*: fitting the STA with a single gammachirp yielded a symmetric function (in *red*) that did not represent the irregularities of the envelope. Two gammachirps (one small earlier one in *blue* and a bigger late one in *green* in **A** *iii*) fitted more faithfully the STA: their superposition (shown in *red* in **A** *iv*) represented better the bimodal STA. **B** and **C**: two other examples of fitting with two components. On the *left* are the two individual components (in *blue* and *green*) and on the *right* their superposition (in *red*). In **A**, **B**, and **C**, the *grey curves* are the raw STAs.

response (computed as the Fourier transform of the STA, see Fig. 2B). At first glance, impulse responses looked similar to what has been reported in the past (de Boer and de Jongh 1978; Carney and Yin 1988; Recio-Spinoso et al. 2005; Fischer et al. 2011; Fontaine et al. 2013): They consisted of a high-frequency oscillation (at around the best frequency of the neuron) modulated in time by an envelope that rose and decayed in a few milliseconds. We fitted analytical functions called gamma chirps to the portion of the STAs where the envelope was higher than 5 % of the maximum, as previously reported (Wagner et al. 2009; Fischer et al. 2011; Fontaine et al. 2013).

The data were fitted to single chirp functions (Fig. 1A (ii)), one with a logarithmic chirp and the other with a linear one (see "Material and Methods"). The envelope was modeled as a gamma function where the order γ determined the symmetry. A small γ yielded an asymmetric envelope with a rising flank faster than the falling flank. γ greater than 15 resulted in a symmetric envelope with Gaussian or Gabor shape (Wagner et al. 2009). Such a fit with a linear frequency glide is shown in Figure 1A (ii). In this example, γ was high, resulting in a symmetric envelope. For the whole sample, simple fits yielded envelopes that widely varied in symmetry with γ=60±42 for the linear case and γ=50±31 for the logarithmic case. Forty-five percent of the envelopes were asymmetric (γ<15) with means γ=6.7±3.1 for the linear and γ=6.1±2.9 for the logarithmic case. The differences in χ_i error were small (median χ_i error for linear glide 5.9 and for logarithmic glide 6.4), but the fits with linear frequency glides were significantly better (Wilcoxon matched-pairs signed-rank test, T=3076, $p=7\times10^{-27}$).

Visual inspection of the population impulse responses suggested that the envelopes were actually not well represented by a single gamma-like function. For example, it can be seen in Figure 1A, B, and C and Figure 2A that the envelopes were bimodal, suggesting that the impulse responses were actually the superposition of two components. To test whether a complex function was effective at representing the impulse responses, we fitted functions consisting of a linear combination of two simple gamma chirp functions. The frequency glides in each function were either both linear, both logarithmic, or one of each. Such fits are shown in Figure 1A (iii), B, and C, which illustrate that each component of the impulse response corresponding to different envelope modes was well fit by a single function. The sum of both functions represented faithfully the whole impulse response (Fig. A (iv) and right panel in B and C). Most (68 %) individual components were asymmetric

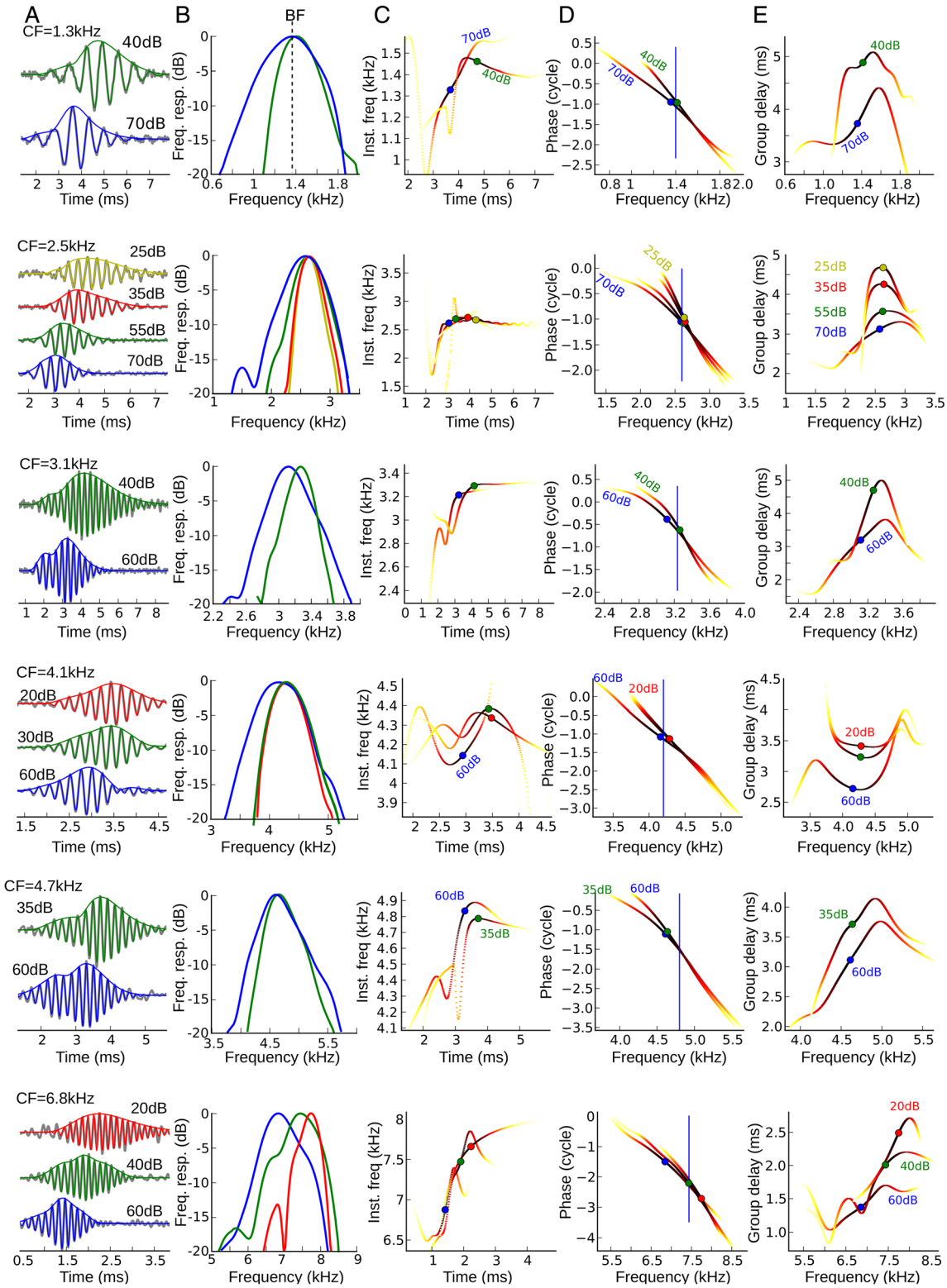

FIG. 2. Impulse response analysis in time and frequency. Each *row* represents a cell, from *lower* (*top*) to *higher* (*bottom*) CF. **A**: impulse responses at different input levels (different colors) plotted as the time inverted version of the STA. Both the fine structure and the envelope of the impulse responses are plotted. **B**: amplitude frequency tuning for the different input levels derived from the raw STAs. **C**: instantaneous frequency at different levels. **D**: phase curves. **E**: group delays. The bullets in **C**–**E** (color-coded by the input level as in **A**) indicate the time where the envelope is maximal (t_{max}), or to BF, respectively. The *curves* in columns **C**–**E** are color-coded with respect to the magnitude of the corresponding envelope with *dark colors* representing higher values.

(γ<15; γ=6.1±2.9). In those examples, which represent a majority of the measurements, it appears therefore reasonable to use double chirps to fit the data.

Transfer Function Analysis

Because the result of the fitting procedure is noiseless, we used it for the analysis as previously reported (Wagner et al. 2009; Fischer et al. 2011; Fontaine et al. 2013). Even though the complex fits were a linear combination of simple time signals, properties of interest such as frequency tuning (Fig. 2B), instantaneous frequencies (Fig. 2C), phase (Fig. 2D), and delay (Fig. 2E) were non-linear functions of the corresponding properties of the simple filters used in the combination. Indeed, even if the Fourier transform was linear, its features phase and instantaneous frequency were not. Therefore, the parameters found by the fitting could not be directly used as previously done (Wagner et al. 2009; Fischer et al. 2011; Fontaine et al. 2013), but the corresponding properties had to be computed numerically. Examples of different features studied in this paper are shown in Figure 2. Each row of Figure 2 shows data from one particular cell. Column A shows impulse responses at different input level, column B the amplitude of the frequency response (derived from the raw STAs), column C the IF, column D the compensated phase, and E the group delay, defined as the negative of the derivative of the phase with respect to frequency. Below, we examine the properties of the transfer function between presented sound and AN responses as a function of BF and input level. Performing the analysis on the fitted STAs is a valid approach as there is a very good correspondence between the basic properties of the raw and fitted STAs: For the impulse responses, compare the grey lines with the colored ones in Figure 1A, B, C and in Figure 2A. For the frequency and phase tuning, compare the grey lines with the colored ones in Figure 3 where it can be seen that the correspondence is generally very good down to −25 dB.

Frequency Tuning

In this section, we characterize the frequency response (Fig. 2B). Detailed comparisons between frequency tunings estimated using tones and noise are shown in Figure 4. For the eight examples shown, there is a good correspondence between both tunings. When the tuning differed, the discrepancy could be explained by the fact that the STAs were estimated using noise presented above threshold, which resulted in wider bandwidth than at threshold (Temchin et al. 2005). For the whole population, BF, defined as the frequency of maximum response in the STA, was highly correlated with the CF (see "Material and Methods" for the definition of CF) (Fig. 5A, R^2=0.98, p=1.43e−230, −0.18+BF*0.97), as would be expected from a quasi-linear system (Recio-Spinoso et al. 2009). Because for a given cell BF can vary with sound level but CF cannot, BF and CF were not exactly identical, especially for higher frequencies. To study the frequency tuning sharpness, we defined a 10-dB bandwidth (BW^{10dB}) as the frequency range where the frequency response (Fig. 2B) was 10 dB lower than the maximum. The resulting BW_{10dB} for all the responses at all BFs is shown in Figure 5B. BW_{10dB} was positively correlated with BF (R^2=0.39, p=1.15e−34, 0.0.23 kHz+BF*0.17). To express the resolution as a unitless value, we derived a Q^{10dB} factor, which was the BW_{10dB} divided by the BF. The results for the whole population are shown in Figure 5C. The Q_{10dB} was slightly positively correlated with BF (R^2=0.11, p=0.005, 3.6+BF*0.2 ms). For comparison, the Q^{10dB} factors of chinchillas (Recio-Spinoso et al. 2005) and cats (van der Heijden and Joris 2003) are also shown. Symmetry of the frequency tuning curves was quantified by comparing the area under the tuning curves (10 dB below the peak) on both sides of the peak. The difference in areas is given by the symmetry index $(B-A)/A+B$), where A is the area on the left side and B the area on the right side of the peak. The symmetry indices, shown in Figure 5D, were overall very low (−0.02±0.15) and slightly positively correlated with BF (R^2=0.21, p= 1.65e−12, −0.43+BF*0.05 ms). This is in agreement with the dependence on BF of the slope ratio of auditory nerve threshold tuning curves measured with tones (Köppl 1997a).

We then characterized the sensitivity of the frequency tuning to input level using the slope of the linear regression of the feature values versus level in decibels. The sensitivity of the BF was estimated as percentage of the CF per 10 dB (Fig. 6A). The BF sensitivity was almost always negative (−1.17±0.99 kHz/10 dB), which means that the filter's BF decreased as the level increased. The BF sensitivity was negatively correlated with BF (R^2=0.2, p=2.38e−6; regression line, 0.25 kHz/10 dB-0.25*BF/10 dB). The BW^{10dB} sensitivity (Fig. 6B) was mainly positive (143±105 Hz/10 dB) and slightly positively correlated with BF (R^2=0.09, p= 0.004, 48 Hz/10 dB+16*BF/10 dB), although large negative values were seen for higher BF. The Q^{10dB} sensitivity (Fig. 6C) was mainly negative (−0.57±0.4/ 10 dB) and was not correlated with BF (R^2=2.3e-5, p=0.93). The symmetry index sensitivity (Fig. 6D) was positive (0.03±0.07/10 dB) and not correlated with BF (R^2=0.002, p=0.4). The frequency tuning example shown in the first row of Figure 2B had a

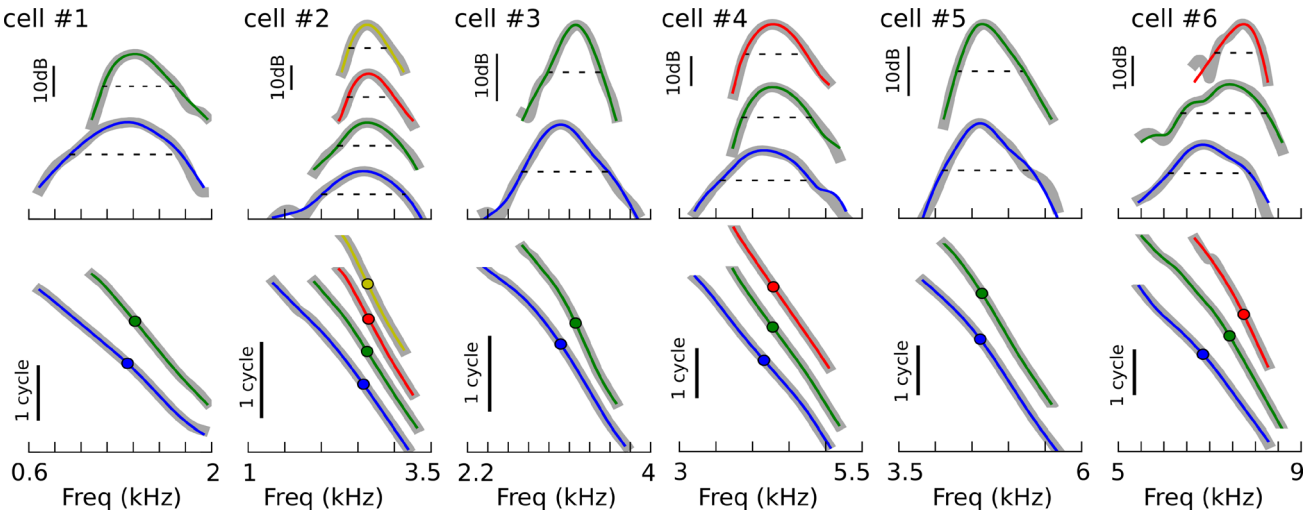

FIG. 3. Comparisons between raw and fitted STA properties. Frequency tuning (*upper panels*) and phase curves (*lower panel*) for the same six ANFs shown in Fig. 2. The *thick gray lines* are the features computed from the raw STA, and the *colored* ones are the features computed from the fitted STAs. Each color represents an input level. The frequency tuning and the phase curves have been shifted for clarity. In the frequency tuning curves, the *horizontal dashed lines* indicate the 10 dB bandwidth.

symmetry index of 0.044, and the one in the second row a symmetry index of 0.017. Those examples are very similar to observations in mammalian STAs: The high-frequency flanks mostly overlap whereas the low-frequency flanks get systematically shallower as the level increases (Moller 1977; Carney and Yin 1988). The STA population exhibited a similar trend.

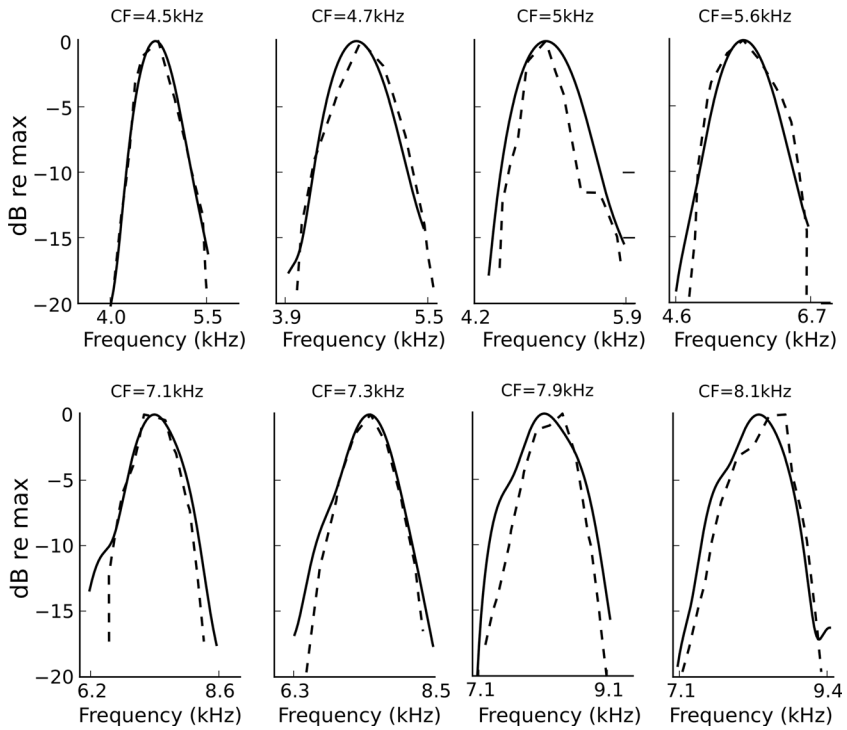

FIG. 4. Comparison between frequency tunings estimated with noises (*solid lines*) and with tones (*dashed lines*). The tones threshold curves are inverted. The curves are normalized so that their maxima are 0 dB. The frequency tuning estimated with noises is derived from the raw STAs.

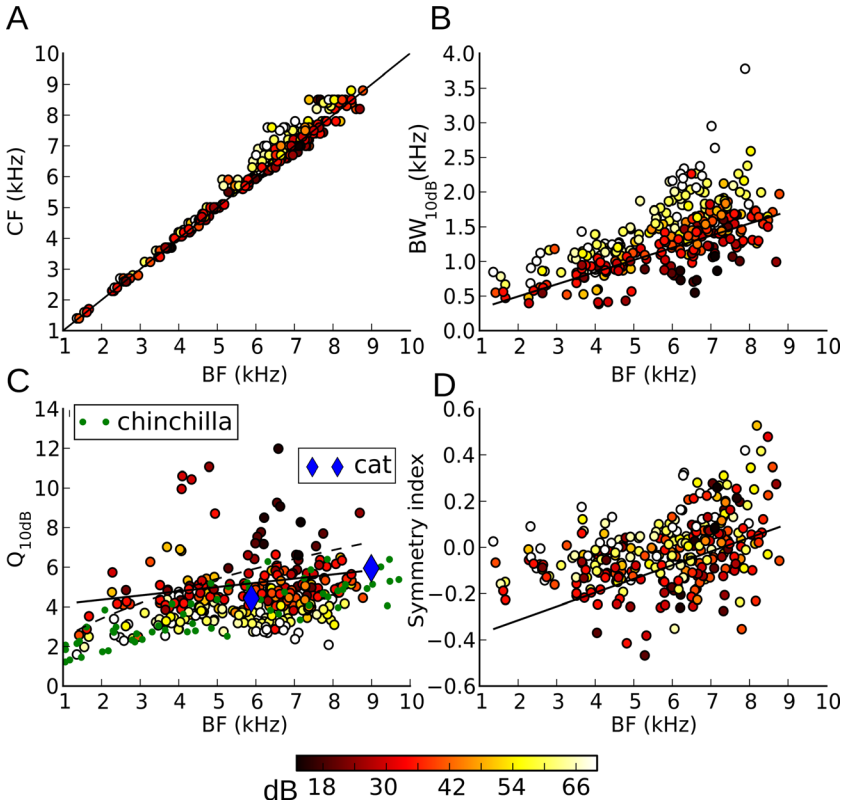

FIG. 5. Frequency tuning at all input levels. Tuning properties as a function of best frequency (BF, frequency where response is maximal). Each *point* represents a response at a given input level which is color-coded. **A**: characteristic frequency (**CF**, estimated via FTC). The *solid black line* is the identity line. **B**: 10 dB band width, **C**: quality factor Q_{10dB}, and **D**: symmetry index (see text). In **B**, **C**, and **D**, the *solid black lines* are the corresponding regression lines. In **C**, for comparison, the Q_{10dB} factors of chinchillas in *green* (Temchin et al. 2005) and cats in *blue* (van der Heijden and Joris 2003) have been superimposed. The *dashed line* is the power fit reported for barn owl Q_{10dB} values using FTC (Köppl 1997a).

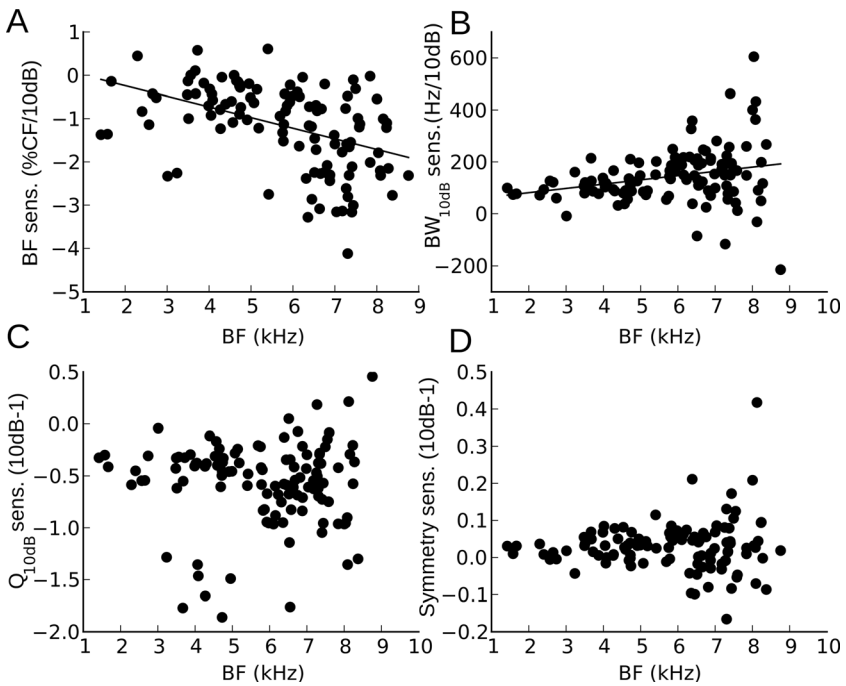

FIG. 6. Frequency tuning sensitivity to input level. Tuning properties as a function of mean BF (averaged across all measured levels). **A**: best frequency sensitivity in percentage of CF per 10 dB. **B**: 10 dB bandwidth sensitivity in Hz per 10 dB. **C**: Q_{10dB} sensitivity. **D**: symmetry index sensitivity. The *solid black lines* are the regression lines.

Instantaneous Frequency

The instantaneous frequency (IF) can be computed from the impulse response (see "Materials and Methods"). In Figure 2C, IF is plotted as a function of time, within the range where the envelope was bigger than 5 % of the maximum. Several examples in Figure 2C showed that IFs increased with time rapidly from the start up to when the envelope was maximal (t_{max}), after which IF reached a plateau. In order to quantify this frequency shift, we computed two parameters per IF function: c_{start} is the rate of change (slope) of the IF between the start of the impulse response and t_{max} and c_{end} is the IF slope between t_{max} and the end of the impulse response. We also computed the overall slope ($c_{overall}$). These features are shown in Figure 7A for $c_{overall}$, Figure 5B for c_{start}, and Figure 7C for c_{end}. $c_{overall}$ (mean 0.27±0.5 ms/kHz) was positively correlated with BF (R^2=0.12, p=1.3e−9, −0.29 ms/kHz+0.05 ms*BF). c^{start} was larger (mean 0.75±2.4 ms/kHz), slightly positively correlated with BF (R^2=0.04, p=0.0003, −0.97 ms/kHz+0.25 ms*BF). c^{end} was smaller (mean 0.11±0.05 ms/kHz) and was slightly correlated with BF (R^2=0.04, p=0.0003). The absolute slope at the start was highly significantly larger than at the end (one-sided paired t test, t=−3.75,p=6.7e−13). The impulse response therefore contained two instantaneous frequency ranges, one steep flank up to BF and one much smaller afterward. One noticeable feature of the different c's is that the variability increased with BF (Fig. 7A, B, and C). The sensitivities of the different slopes to input level are shown in Figure 7D, E, and F. None of them were correlated with BF (all p>0.01). The

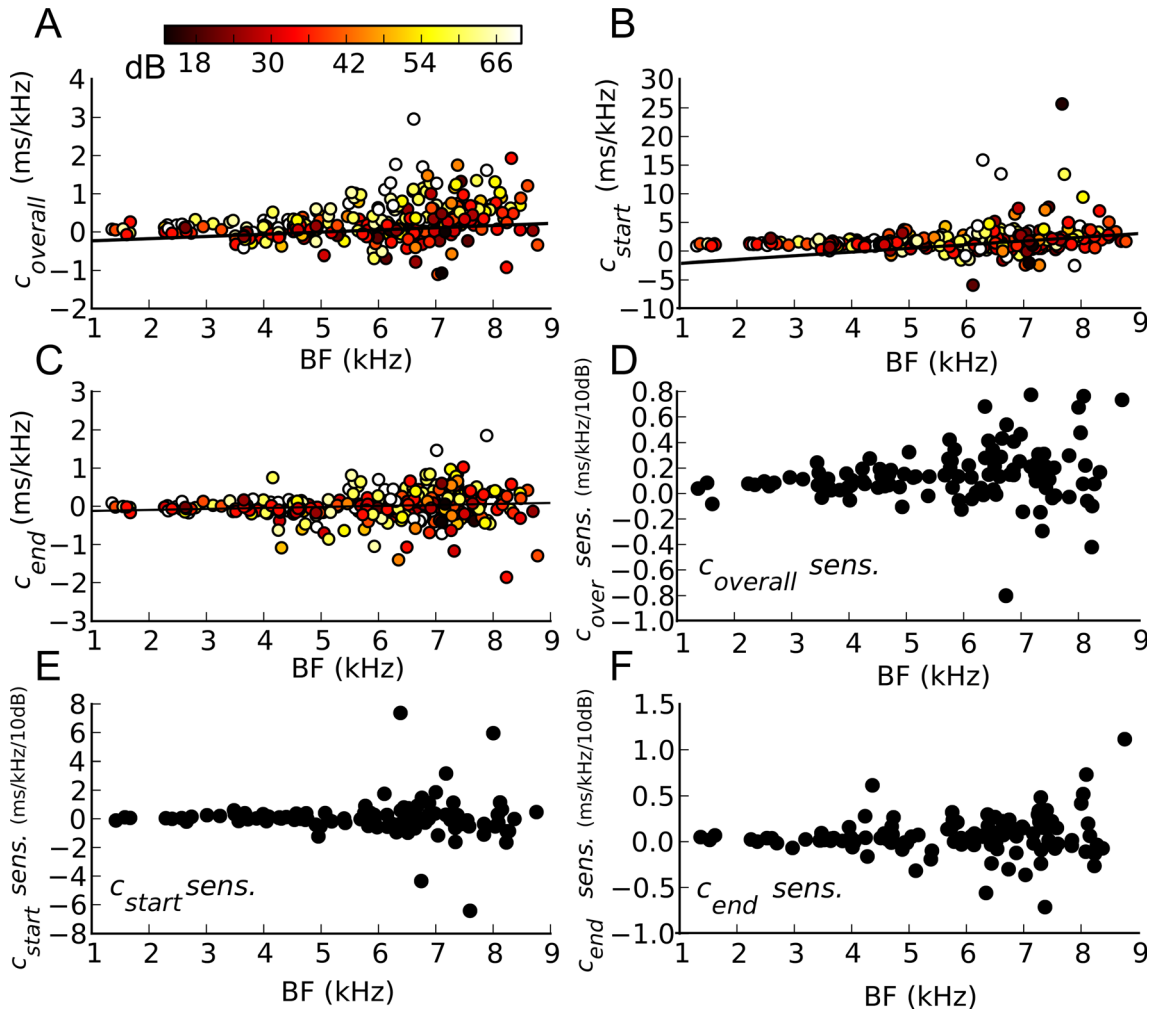

FIG. 7. Instantaneous frequency slope. **A**, **B**, and **C**: each point represents the slope (in milliseconds per kilohertz) of the instantaneous frequency for one particular unit at one particular input level. The input level is color-coded. **A**: $c_{overall}$: slope calculated along the entire impulse response. **B**: c_{start}: slope calculated from the start of the impulse response up to the maximum of its envelope. **C**: c_{end}: slope calculated from the maximum of the impulse response envelope up to its end. **D**, **E**, **F**: sensitivity of the slopes to input level (in milliseconds per kilohertz per 10 dB) for $c_{overall}$ (**D**), c_{start} (**E**), and c_{end} (**F**). The *solid lines* are regression lines to the corresponding data.

distribution of c^{overall} sensitivity (mean 0.11±0.21 ms/kHz/10 dB) had a mean significantly different from 0 (two-sided *t*test t=5.5, p<1.3e−25) which was not the case for c_{start} sensitivity (mean 0.06±1.3 ms/kHz/10 dB, two-sided *t*test t=0.49, p=0.6) and c_{end} sensitivity (mean 0.05±0.22 ms/kHz/10 dB, two-sided t-test t=2.6, p=0.011). Again, the variability of those sensitivities increased with BF.

To compare IF slopes independently of frequency, we expressed them in unitless values (Recio et al. 1998; Shera 2001; Recio-Spinoso et al. 2005). To do so, the slope was divided by BF^2. The three resulting slopes were plotted in Figure 8. The three slopes were very small (c^{overall}, mean 0.01±0.01; c_{start}, mean 0.02±0.05; c_{end}, mean −0.001±0.01) and did not depend on BF (c_{overall}, R^2=0.0002, p=0.78; c^{start}, R^2=0.02, p=0.43; c^{end}, R^2=0.03, p=0.01). In order to compare the barn owl IF profiles with mammalian data (chinchilla, Recio-Spinoso et al. 2005), we plotted the IF slope means as a function of BF for the two species (Fig. 8D). Recio-Spinoso et al. (2005) and Temchin et al. (2011) computed the slope from the first STA minimum up to BF which corresponds to our c^{start} (Fig. 8C). The slopes in barn owl were one order of magnitude lower than in chinchilla.

We tested whether the instantaneous frequency was related to the symmetry of the amplitude of the frequency response as proposed by different authors (Tan and Carney 2003; Temchin et al. 2011). In particular, the polarity of any asymmetry should predict the polarity of the glide slope. We plot in Figure 9A the slope c_{overall} (in milliseconds per kilohertz) as a function of the frequency tuning symmetry. Both were correlated (R^2=0.2, p=1.97e−10). It has also been proposed that dependence of BF on input level (Fig. 6A) can be due to the presence of a non-zero glide slope in the impulse response (Tan and Carney 2003; Wagner et al. 2009). The idea is that if an increase in input level shifts the impulse response envelope to earlier time (see following section) the presence of a non-zero IF slope will set the maximum of the envelope (hence BF) to a lower value if the slope is downward and vice versa. This prediction was verified in our data as the mean c^{overall} (taken over all levels presented to a cell) was correlated with the BF sensitivity to input level (Fig. 9B, R^2=0.28, p=7.3e−9).

Phase and Delay Analysis

We next analyzed the phase-frequency curves of the impulse responses, like those shown in Figure 2D. In order to zoom in on fine details, those phase curves were compensated for the delay corresponding to the

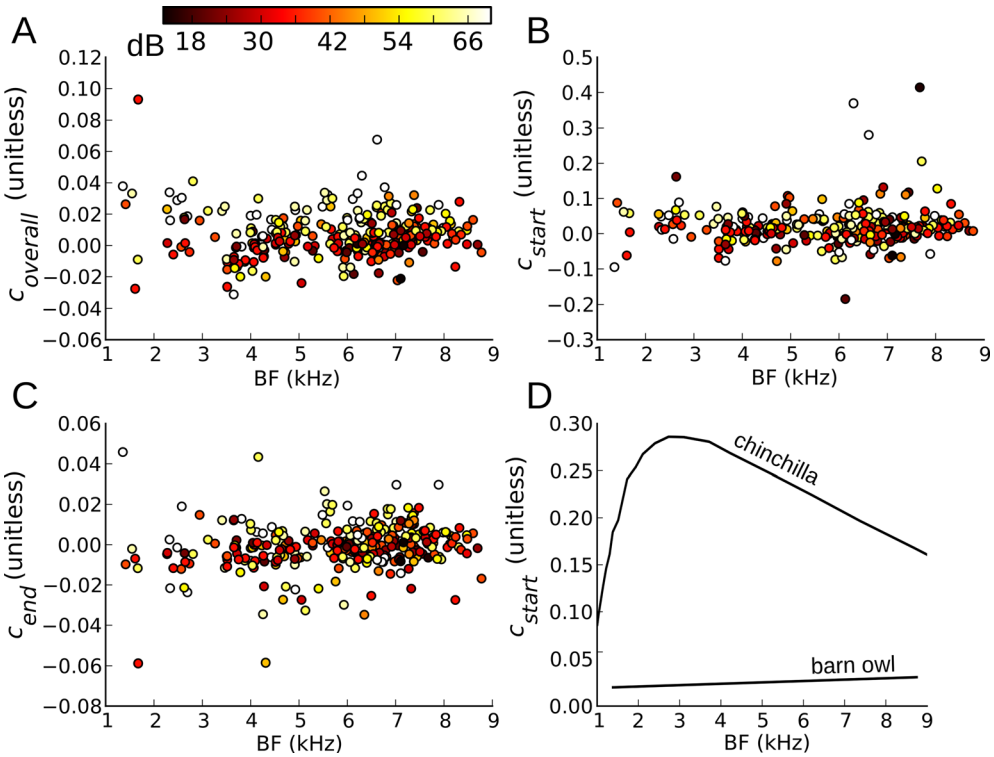

FIG. 8. Unitless instantaneous frequency. To express the slopes in unitless values, they were normalized by BF^2. **A**, **B**, and **C**: each point represents the slope of a given impulse response at a certain input level (color-coded) for each cell along the BF axis, **A**: c^{overall}, **B**: c_{start}, **C**: c_{end}. **D**: the regression line of $c_{\text{start}}t$ in **B** is compared with the c_{start} of chinchilla (Recio-Spinoso et al. 2005).

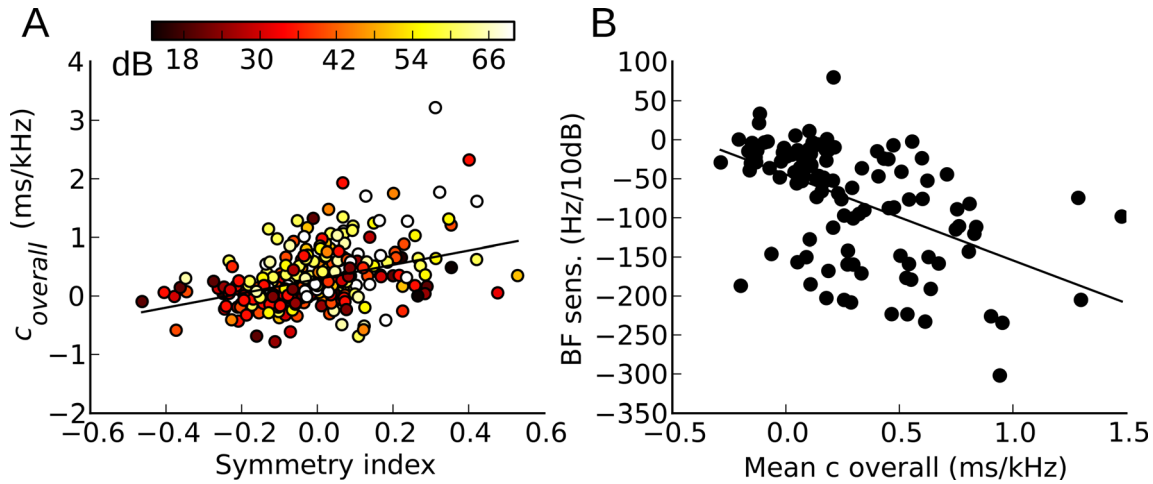

FIG. 9. Relationship between IF slope and frequency tuning symmetry and BF sensitivity to input level. **A**: IF overall slope versus the symmetry index of the frequency tuning. **B**: BF sensitivity to input level versus the mean of IF slope across all input levels for a given cell. The *solid lines* are the regression lines in both panels. In **A**, the regression line is made on all levels.

onset delay at their lowest input level (a line with a slope corresponding to this delay is subtracted from the initial phase curve). There was variability in their shape. Most of them departed from a straight line. Some were concave upward, some downward, and some changed concavity below and above BF. It was suggested (van der Heijden and Joris 2006) that there is a relationship between concavity and the shape of the IF function. Indeed, as can be seen in Figure 10B, a negative IF slope yielded a downward concavity whereas a positive IF slope yielded an upward concavity (see caption of Figure 10 for details of the filters design).

It was experimentally observed, first in cat AN (Anderson et al. 1971) and many times afterwards in mammalian AN and basilar membrane responses (e.g. Recio-Spinoso et al. 2005; Palmer and Shackleton 2009; Versteegh et al. 2011), that an increase in input level induces a phase lag below CF and a phase lead above CF. Our results (Fig. 2C) are consistent with this finding. The hypothesis of exact CF pivoting, introduced as a simplification in subsequent modeling studies (Carney and Yin 1988), states that, for different input levels, the phase curve pivots around CF, leaving the phase at CF constant. It was proposed that this behavior is due to a change in damping properties of the filter (Carney 1993). Note that the degree of damping is inversely proportional to the quality factor; a filter with a very high-quality factor will have little damping, i.e., it will ring for a very long time. The hypothesis of exact CF pivoting is illustrated in Figure 10A. The phase curves at different levels from the cells in Figure 2 are replotted in Figure 11 in zoomed versions. Some cells (cell #5) had phase curves more or less consistent with the hypothesis while most others did not. In other cases, the curves for a given cell did not even intersect at the same frequency (cell #4 and #6). Figure 10C shows that this departure is concomitant with the presence of non-zero IF slopes. Indeed, different Q_{10dB} values (corresponding to different degrees of damping) and a non-zero IF slope yielded phase-frequency curves that did not intercept at any frequency. To quantify the degree of "non-exact CF pivoting," we calculated, for pairs of phase-frequency curves at different input levels in a given cell, the distance (in percent of CF) at CF. Note that a distance of zero means that the phase at CF was the same for both input levels. The results are shown in Figure 12A for all cells. The degree of non-exact CF pivoting was different from zero for most of the cells (mean 8±10 % of CF) and was mainly positive, i.e., the phase curves intersected above CF for lower CFs (CF< 4 kHz), while some of them were negative for higher CFs. The degree of non-exact CF pivoting was slightly correlated with BF (R^2=0.1, p=0.002).

The group delay, defined as the negative of the derivative of the phase with respect to frequency, is a widely used measure of the transmission time between outer ear and AN fibers (Köppl 1997b; Recio-Spinoso et al. 2005; Versteegh et al. 2011). Because most of the phase–frequency curves were non-linear (Fig. 2D), the group delay functions were frequency-dependent (Fig. 10B). Those functions were complex, sometimes having maxima at frequencies other than BF (the colored bullets representing BF in Figure 2E are generally not at the same frequency that the maximum group delays). We quantified this effect by computing the distance between the frequency $f_{gd\max}$ where the group delay is maximal and BF, for all responses. The results are shown in Figure 12B. For

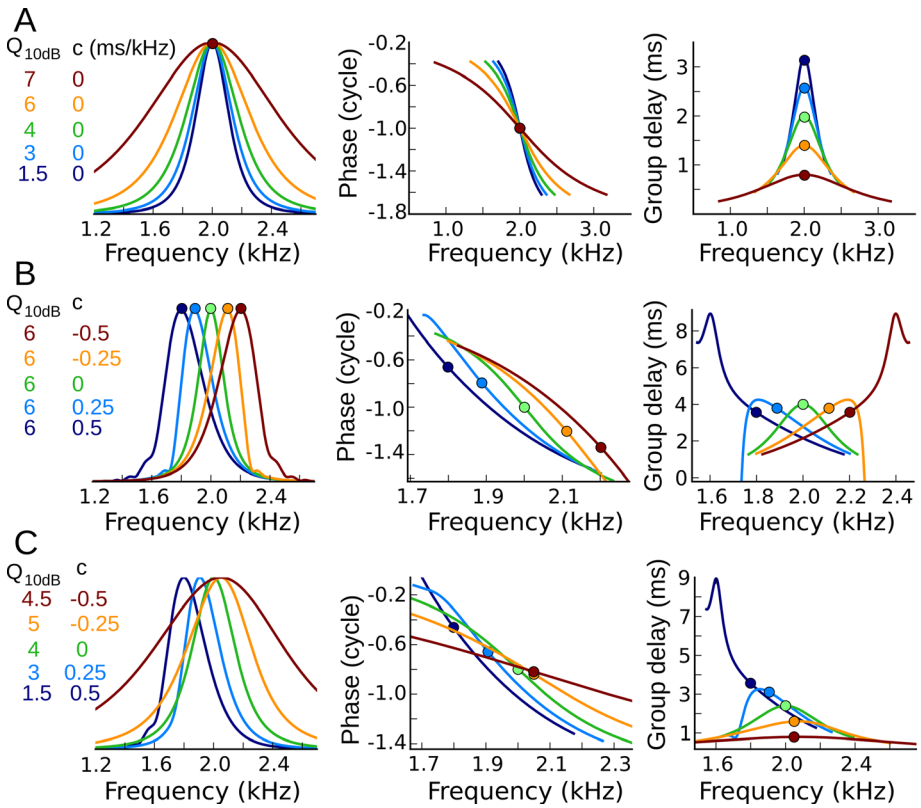

FIG. 10. Schematic illustration of the effect of damping and IF slope on filter properties. **A**: the IF slope was set to zero, and the Q_{10dB} factors varied from 1.5 to 7. **B**: The Q_{10dB} was constant, and the IF slope varied. **C**: Both the Q_{10dB} factor and the IF slope varied. The *first column* shows the normalized frequency response, the *second column* the phase, and the *third column* the group delay as a function of frequency. The colors correspond to the values of Q_{10dB} and c given on the *left*. The bullets are placed at BF. The filters used were a linear gammachirp filters (Eq. 1). For all examples, the starting frequency f_0 was 2 kHz, the filter delay t_0 was 0.5 ms, the order of the gamma envelope was 4, the phase θ was 0. In **A**, the glide slope c is fixed to zero, and the Q_{10dB} factor varied by varying τ from to 0.2 to 1 ms in step of 0.2 ms. In **B**, τ was fixed to 0.8 ms and c varied from −0.5 to 0.5 kHz/ms. In **C**, both τ and c were varied.

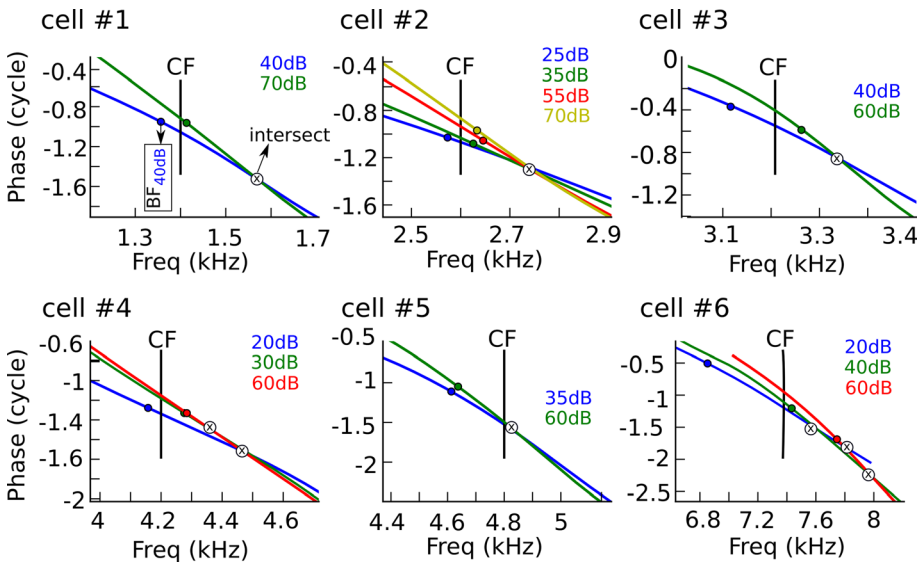

FIG. 11. Pivoting analysis: Phase curves of six cells (the same as the one shown in Fig. 2) for different input levels (the colors of the lines correspond to a certain level). The *vertical black line* is the characteristic frequency of the cell. The *filled bullet* on the phase curves is the best frequency at a given input level (color-coded). The *crosses in a white circle* represent intersection points between two or more phase curves.

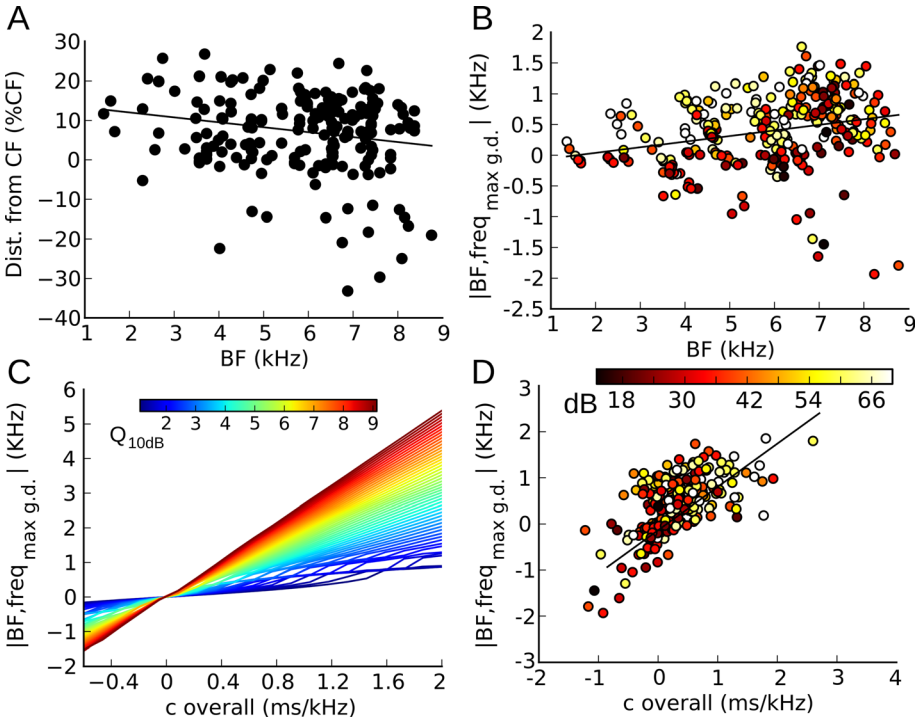

FIG. 12. Hypothesis of exact CF pivoting. **A**: distance of the intersection of a pair of phase curves (given in percentage of CF), as a function of BF. **B**: distance (in Hertz) between BF and the frequency where the group delay was maximal for all responses, as a function of BF. **C**: Predicted distance (in Hertz) between BF and the frequency where the group delay was maximal, as a function of *c*, using simulated data with an analytical filter with a linear IF. The CF of the filter was set at 2 kHz. Changing Q_{10dB} from 1 to 9 yielded the different lines (color-coded). **D**: plotting the same as in **C**, for our data set. In **A**, **B**, and **D**, the *solid black lines* are the regression lines. **B** and **D**: the regression line is made on all levels.

most of the responses, $f_{gd\max}$ did not coincide with BF (mean distance 385±579 Hz). The distance range increased with BF. To explain this behavior, we went back to our simple analytical filter analysis. It can be seen in Figure 10B that the presence of non-zero IF slopes moves the frequency where the group delays is maximum away from BF. Having different IF slopes and Q_{10dB} factors results in complex group delay functions (Fig. 10C). In Figure 12C, using the analytical filters, we plot the distance between BF and $f_{gd\max}$ as a function of IF slope for different Q_{10dB} 's (Fig. 12C). The relationship between glide slope *c* and the distance is linear with a slope that depends on damping. Similarly, distance and c_{overall} were correlated for our sample (Fig. 12D; R^2=0.25, p=1.7e−16).

The group delays near BF are plotted in Figure 13A, where each point is color coded according to which owl it was measured from. It is obvious that there was a large variance of group delays in the higher frequency range (BF>4 kHz). This large variance stemmed largely from inter-individual differences in group delays. In particular, datasets from two individuals differed by almost 1 ms from all others. We can rule out sound level as the major source of differences as similar plots at a given input level showed the same clustering. It is well known, however, that increasing sound level leads to shorter group delays (Köppl 1997b; Temchin and Ruggero 2010; Versteegh et al. 2011), and this was also evident in the current dataset (−166±90 μs/10 dB). Therefore, in order to perform a valid comparison with data reported for mammals, we plot the power law regression of the barn owl group delays together with those of two mammalian species, chinchilla (Recio-Spinoso et al. 2005) and gerbil (Versteegh et al. 2011) (all obtained close to their respective thresholds). While the barn owl responses followed the same trend, i.e., the delays decreased with BF, the group delays were greater than in the mammalian species.

The fact that delays could depend on input level is very important for interaural time difference (ITD) processing (Michelet et al. 2012), for which the barn owl is a specialist (Carr and Konishi 1990). In the barn owl, ITD processing is thought to be based on a cross correlation (Fischer et al. 2008). In particular, the ITD curve, i.e., the firing rate of an ITD sensitive neuron as a function of ITD, is well approximated by the cross-correlation of the STAs from both sides (not taking into account internal delays). ITD curves take the shape of quasi-periodic functions characterized by a fine structure and an envelope, consistent with the

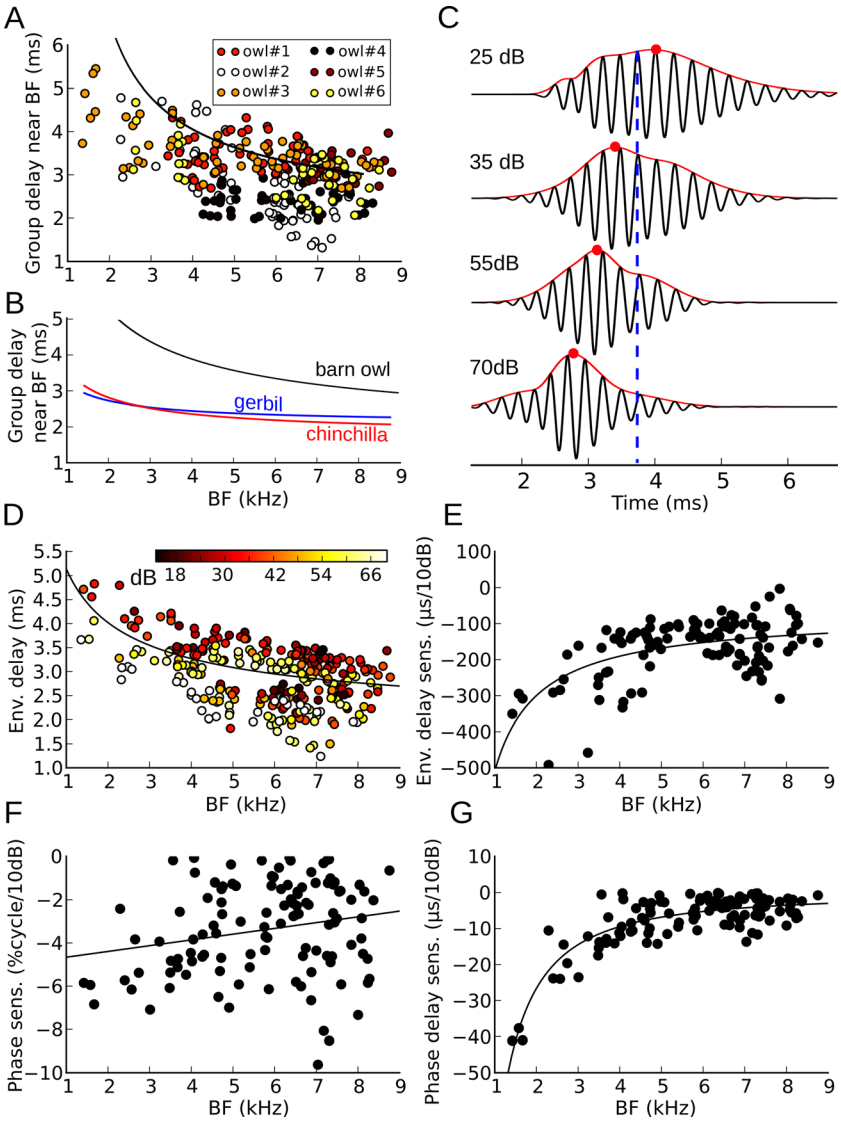

FIG. 13. Response delay analysis. **A**: near BF group delays for the six individual owls (each shown with a different color). **B**: comparison with different mammalian species of power law fits of near BF group delay for chinchilla (Fig. 15B of Recio-Spinoso et al. 2005) and gerbil (Fig. 6B of Versteegh et al. 2011). **C**: illustration of the computation of envelope and fine structure delays. *Black curves* show the fine structure, *red* ones the envelope. The *red point* indicates the envelope delay (where the envelope is maximal). *Blue dashed line* falls at one of the peak of the response at the lowest level. **D**: envelope delays versus BF for all responses (input level is color-coded). **E**: envelope delay sensitivity to input level in microseconds per 10 dB, as a function of BF. **F**: phase sensitivity in percentage of cycle per 10 dB, as a function of BF. **G**: phase delay sensitivity in microseconds per 10 dB, as a function of BF.

fine structure and envelope of the STAs of the inputs from both sides (Fischer et al. 2008). The ITD where the envelope of the ITD curve is maximal is the difference between the STA envelope delays from both sides (red point in Fig. 13C). On the other hand, the ITD that induces peaks in the ITD curve is the time difference between the fine structure of STAs of both sides and phase-equivalents every period of BF (Fig. 13C where the dashed blue line represents one peak maximum of the lowest level response). If the monaural envelope delays were very sensitive to input level, the position of the maximum of the envelope of the ITD curve would depend on interaural level difference (ILD). If the monaural fine-structure (phase) delays were very sensitive to input level, the position of the peaks of the ITD curve would depend on ILD. Both the sensitivity of envelope delays (Fig. 13E) and phase delays to input level were computed. The phase delay is shown in cycles per 10 dB in Figure 13F and in microseconds in Figure 13G. Comparing Figure 13E and G, we can conclude that the phase delay sensitivity to input level is more than one order of magnitude smaller than the envelope delay sensitivity.

DISCUSSION

In this paper, we studied, for the first time in an avian species, the properties of the AN impulse response derived from spike triggered averages. In our dataset, the relationship between the impulse response properties as well as their dependence on input level can be modeled using a linear filter approach. While some conclusions were consistent with findings in mammals, others were clearly different, in particular, the shape of the STAs and the rate at which the instantaneous frequency of the impulse response changed. Also, we showed that phase–frequency curves at different sound levels did not always intersect at a common point as previously shown in mammals (Anderson et al. 1971; Recio-Spinoso et al. 2005; Versteegh et al. 2011). We discuss the possible meaning of the differences and similarities encountered.

Shape of Impulse Response

Whereas simple functions have previously been used to fit avian STAs from the responses of brainstem neurons (Wagner et al. 2009; Fischer et al. 2011), we showed here that, in some cases, the impulse response envelope had a more complex bimodal shape. This fact was previously mentioned in Wagner et al. (2009) but represented a small subset of the recordings. Those complex STAs are transmitted to subsequent centers of the auditory pathway as they can be found in nucleus magnocellularis (Fig. 14A), which is one synapse away from AN, and in nucleus laminaris, two synapses away (Fig. 14B).

In the mammalian auditory system, multi-component impulse responses were, to our knowledge, only reported in STAs when clicks were used. Clicks trigger more non-linear processes, as shown for the chinchilla basilar membrane, where a sub-population showed double-mode responses (Recio et al. 1998), and cat auditory-nerve fibers (Lin and Guinan 2004). In those cases, however, there was a noticeable difference compared with the barn owl: The smaller component consisted of a later ringing, unlike the small early and time-restricted components in our dataset. The bimodal characteristics of the STAs might be due to the fact that two modes of cochlear excitation are present (Lin and Guinan 2004; Guinan and Cooper 2008; Guinan 2012). Why this phenomenon is observed in STAs in barn owl while only for clicks in mammals is unclear.

Frequency Tuning

Neurons tuned to higher frequencies had a greater BF sensitivity to input level (Fig. 6A). This is similar, at least qualitatively, to what happens in the base of the mammalian cochlea. Also, frequency tuning bandwidth increased with BF (Fig. 5B) as reported in mammals (Rhode and Smith 1985; Mc Laughlin et al. 2007). Also like in mammals (de Boer and de Jongh 1978; Carney and Yin 1988; Mc Laughlin et al. 2007), BW_{10dB} increased with input level (Fig. 6B). The quality factor Q_{10dB} increased with BF (Fig. 5C), as reported with tones in owls (Köppl 1997a) or with other stimuli in mammals (Shera and Guinan 2003) and decreased with input level (Fig. 6C) (Recio-Spinoso et al. 2005), i.e., tuning is sharper for softer sounds. The Q_{10dB} factors for the chinchilla plotted in green in Figure 5C correspond to low input levels (just above threshold (Recio-Spinoso et al. 2005)). As they are similar to Q_{10dB} factors of owls at higher input levels, we can conclude that the tuning, in general, is sharper in owl than in chinchilla. Even though the frequency tuning of the cochlear filters is more symmetric than in mammals (Köppl 1997a), we found that the tuning became more asymmetric as CF increased (Fig. 5D), like

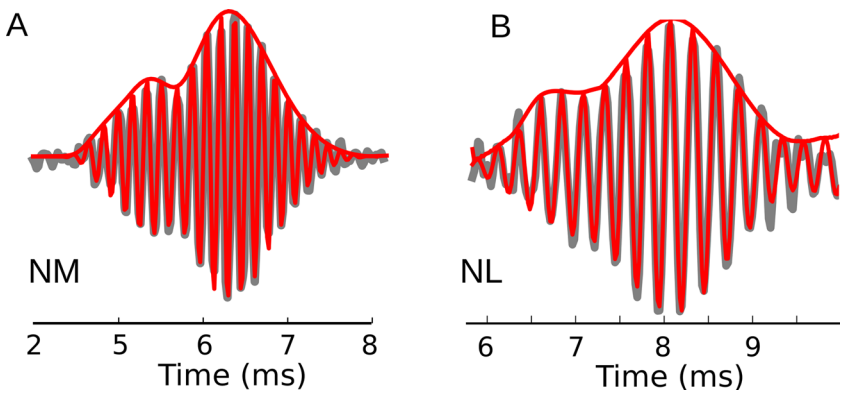

FIG. 14. Impulse responses in subsequent centers. Complex STAs with bimodal envelope can be found in subsequent auditory centers. **A**: STA computed from a nucleus magnocellularis response, which is one synapse further than AN. **B**: STA computed from a nucleus laminaris response, which is two synapses away from AN. *Red* and *gray curves* represent the measured and fitted STA, respectively.

in mammals (van der Heijden and Joris 2003). BF decreased with increasing input level (Fig. 6A) more systematically than in cat. We showed (Fig. 9B) that the presence of a non-zero glide slope coupled with large sensitivity of group delays to input level could explain this non-linearity in the context of a linear system as in Tan and Carney (2003).

Instantaneous Frequency of the Impulse Response

The AN IF functions were not linear like in cat STAs (Carney et al. 1999) or what has been reported from brainstem STAs in barn owls (Wagner et al. 2009; Fischer et al. 2011); there was a steep change up to BF, followed by a slower component (Fig. 2C). Unlike previously reported in the mammalian AN (Carney et al. 1999; Shera 2001) but consistent with basilar membrane measurements (Recio-Spinoso et al. 2009), the overall glide slopes were dependent, albeit weakly, on input level, especially for BF>4 kHz (Fig. 7D–F). Our results would thus predict that the monaural inputs from AN (via nucleus magnocellularis) to the binaural neurons in the nucleus laminaris would change glide slopes differently on each side for a non-zero ILD. Whether the matching input properties of binaural neurons (Fischer et al. 2011) hold for non-zero ILD is an open question.

Asymmetries in the frequency tuning of linear systems are associated with phase modulation (e.g., frequency glides) in impulse responses (Papoulis 1977; Recio and Rhode 2000; Tan and Carney 2003). In the chinchilla, it has been shown (Temchin et al. 2011) that, for CFs below 1.5 kHz, there is good correspondence between symmetry and glide slope but, at BF above 1 kHz, the frequency tuning remains invariant while the glide slope decreases. We showed (Fig. 9A) that the symmetry index of barn owl AN STAs was correlated with the IF slope along the entire tonotopic axis.

Perhaps the most striking feature of the barn owl IFs (Fig. 8D) is that the slopes were one order of magnitude smaller than for mammals. According to Tan and Carney (2003) and Temchin et al. (2011), this is consistent with the observation that avian tuning curves tend to be more symmetric than mammalian ones (Manley et al. 1985), which is also true for the barn owl (Köppl 1997a). One theory about the origin of frequency glides stipulates that glides are a consequence of the dispersive properties of the travelling wave (Shera 2001): Because different frequencies do not travel at the same velocity, different components will not arrive at the same time, leading to IF glides. According to this theory, our results then predict that, should a travelling wave exist in the owl, it should be a lot less dispersive than its mammalian counterpart. This is entirely plausible, as the nature of cochlear micromechanics in birds remains poorly understood. The only direct observations of basilar membrane motion in the pigeon concluded that a travelling wave was present. However, its frequency resolution and sensitivity did not approximate the known selectivity and sensitivity at the neural level (Gummer et al. 1987). This suggests that basilar-membrane motion does not reflect the stimulation ultimately driving the tall hair cells' transduction in birds. It does not rule out, though, the possibility of additional and more sensitive travelling-wave like motion supported by other structures, e.g., the tectorial membrane. Along a similar line, techniques of extracting an underlying compressive nonlinearity from auditory nerve rate-level functions suggested, from the direct comparison with equivalent mammalian data, a very locally-restricted action of amplification in the avian basilar papilla (reviewed in Köppl 2011). Although this analysis cannot conclude anything specific regarding the presence or absence of travelling waves, it once more points to a different mode of operation of avian and mammalian cochleae. The strongest indirect evidence for some kind of travelling wave in birds remains the significant and frequency-dependent phase accumulation, or group delay, as shown again here (Fig. 13). However, as pointed out before (Ruggero and Temchin 2007), the exact physical nature of this travelling wave need not be, and we emphasize here is unlikely to be, the same as in the mammalian cochlea.

Another theory about the origin of the glides relies on multiple local excitation drives (Lin and Guinan 2004) and could be more consistent with the barn owl data as many AN STAs clearly contained at least two basic components, suggesting that multiple resonances are present.

Phase and Delay

In mammals, it has been shown that the phase curves were concave upward for CF<1 kHz and downward above (van der Heijden and Joris 2006; Temchin et al. 2011; Versteegh et al. 2011). As shown in Figure 10B, the concavity is related to the sign of the IF slope: A positive slope yields an upward concavity. In the current dataset, while this relationship seemed to hold, there was no transition along the tonotopical axis between upward and downward, as observed in mammals.

The fact that the hypothesis of exact CF pivoting, which posits that when level changes, the phase curve pivots around CF, does not always hold was already reported for one ANF in Anderson et al. 1971. Since then, it has been reported many times in mammals (e.g.. Recio-Spinoso et al. 2005; Palmer and

Shackleton 2009; Versteegh et al. 2011) and in the owl AN with tones (Köppl 1997a, b, c). We corroborated those results for barn owl STAs (Fig. 10A). While those results go against simple filter models with damping that changes with input level (Fig. 10A) (Carney and Yin 1988; Carney 1993), we showed that the presence of a non-negative IF slope is concomitant with the deviation from the hypothesis of exact CF pivoting (Fig. 10B and C).

Any non-symmetric impulse response has non-linear phase curve (Papoulis 1977), which means that the group delay depends on frequency. In the hypothesis of exact CF pivoting, the maximum group delay is independent of the damping (Fig. 10A). Nevertheless, if the IF slope is non-negative, the maximum group-delay is not at BF (Fig. 10B and C). Again, we have shown, using analytical filters (Fig. 10C) and measured data (Fig. 10D), that this effect is concomitant with the presence of non-zero IF slopes. In other words, cochlear filtering could still be consistent with simple filter theory taking into account phase modulation.

The near BF group delay function (Fig. 13B) of the barn owl resembled those of different mammalian species in that it decreased with CF following a power law. This is in apparent contrast to the very unusual tonotopic representation of frequencies along the barn owl's basilar papilla, where frequencies between 4 and 10 kHz are disproportionately overrepresented in terms of cochlear length, termed an auditory fovea (Köppl et al. 1993). If a uniformly propagating travelling wave were present, the delays along the tonotopic axis should reflect this drastically changing representation across frequencies (Köppl 1997b). However, this did not appear to be the case. Instead, we observed (Fig. 13A) that, in the foveal frequency range, there was substantial variability of the delay range between individual owls. Also, the near-BF delays were greater for all CF than in any mammalian species. These longer delays are consistent with sharper tuning in barn owl.

The fact that the relevant delays for ITD processing might be dependent on input level means that ITD processing would depend on ILD. We showed that the envelope delay of the monaural input depended greatly on the input level (Fig. 13E, from 100 µs/10 dB up to 500 µs/10 dB, consistent with delays retrieved from cochlear evoked potentials (Köppl and Gleich 2007)). The phase delay was one order of magnitude more robust (Fig. 13F, around 10 µs/10 dB). These results are consistent with measurements in ITD sensitive neurons (Peña et al. 1996; Viete et al. 1997; Wagner 2005) and show that the phase invariance to input level is already present at the AN level. In cat, the envelope delay to input level is more robust to change in sound level than for the barn owl (Michelet et al. 2012). The difference between owls and cats appears adaptive considering that, in the owl, the fine structure is used for ITD processing across the whole hearing range whereas in cat only envelope timing is used for ITD processing at frequencies above the limit of phase locking.

ACKNOWLEDGMENTS

Work supported by a European Community Marie Curie fellowship (PIOF-GA-2011-300753) for B.F., by the Deutsche Forschungsgemeinschaft (SFB/TRR31 "Active Hearing") to CK, by the National Institute of Health (DC007690) to JLP. The authors would like to thanks B. Fischer for helping with the statistics.

Conflict of Interest

The authors declare that they have no conflict of interest.

REFERENCES

ANDERSON DJ, ROSE JE, HIND JE, BRUGGE JF (1971) Temporal position of discharges in single auditory nerve fibers within the cycle of a sine-wave stimulus: frequency and intensity effects. J Acoust Soc Am 49:1131–1139. doi:10.1121/1.1912474

CARNEY LH (1993) A model for the responses of low-frequency auditory-nerve fibers in cat. J Acoust Soc Am 93:401

CARNEY LH, YIN TC (1988) Temporal coding of resonances by low-frequency auditory nerve fibers: single-fiber responses and a population model. J Neurophysiol 60:1653–1677

CARNEY LH, MCDUFFY MJ, SHEKHTER I (1999) Frequency glides in the impulse responses of auditory-nerve fibers. J Acoust Soc Am 105:2384

CARR C, KONISHI M (1990) A circuit for detection of interaural time differences in the brain stem of the barn owl. J Neurosci 10:3227–3246

DE BOER E, DE JONGH HR (1978) On cochlear encoding: potentialities and limitations of the reverse-correlation technique. J Acoust Soc Am 63:115–135

DE BOER E, NUTTALL AL (1997) The mechanical waveform of the basilar membrane. I. Frequency modulations ("glides") in impulse responses and cross-correlation functions. J Acoust Soc Am 101:3583–3592

FISCHER BJ, CHRISTIANSON GB, PEÑA JL (2008) Cross-correlation in the auditory coincidence detectors of owls. J Neurosci 28:8107–8115. doi:10.1523/JNEUROSCI.1969-08.2008

FISCHER BJ, STEINBERG LJ, FONTAINE B ET AL (2011) Effect of instantaneous frequency glides on interaural time difference processing by auditory coincidence detectors. Proc Natl Acad Sci 108:18138–18143. doi:10.1073/pnas.1108921108

FONTAINE B, BENICHOUX V, JORIS PX, BRETTE R (2013) Predicting spike timing in highly synchronous auditory neurons at different sound levels. J Neurophysiol 110:1672–1688. doi:10.1152/jn.00051.2013

FONTAINE B, MACLEOD KM, LUBEJKO ST ET AL (2014) Emergence of band-pass filtering through adaptive spiking in the owl's

cochlear nucleus. J Neurophysiol 12:430–445. doi:10.1152/jn.00132.2014

Fuchs PA, Nagai T, Evans MG (1988) Electrical tuning in hair cells isolated from the chick cochlea. J Neurosci 8:2460–2467

Guinan JJ Jr (2012) How are inner hair cells stimulated? Evidence for multiple mechanical drives. Hear Res 292:35–50. doi:10.1016/j.heares.2012.08.005

Guinan JJ Jr, Cooper NP (2008) Medial olivocochlear efferent inhibition of basilar-membrane responses to clicks: evidence for two modes of cochlear mechanical excitation. J Acoust Soc Am 124:1080–1092. doi:10.1121/1.2949435

Gummer AW, Smolders JW, Klinke R (1987) Basilar membrane motion in the pigeon measured with the Mössbauer technique. Hear Res 29:63–92

Irino T, Patterson RD (2001) A compressive gammachirp auditory filter for both physiological and psychophysical data. J Acoust Soc Am 109:2008

Kijewski-Correa T, Kareem A (2006) Efficacy of Hilbert and wavelet transforms for time-frequency analysis. J Eng Mech 132:1037–1049

Köppl C (1997a) Frequency tuning and spontaneous activity in the auditory nerve and cochlear nucleus magnocellularis of the barn owl *Tyto alba*. J Neurophysiol 77:364–377

Köppl C (1997b) Phase locking to high frequencies in the auditory nerve and cochlear nucleus magnocellularis of the barn owl, *Tyto alba*. J Neurosci 17:3312–3321

Köppl C (1997c) Number and axon calibres of cochlear afferents in the barn owl. Aud Neurosci 3:313–334

Köppl C (2011) Birds—same thing, but different? Convergent evolution in the avian and mammalian auditory systems provides informative comparative models. Hear Res 273:65–71. doi:10.1016/j.heares.2010.03.095

Köppl C, Gleich O (2007) Evoked cochlear potentials in the barn owl. J Comp Physiol A Neuroethol Sens Neural Behav Physiol 193:601–612. doi:10.1007/s00359-007-0215-0

Köppl C, Gleich O, Manley GA (1993) An auditory fovea in the barn owl cochlea. J Comp Physiol A 171:695–704. doi:10.1007/BF00213066

Lewis ER, Henry KR, Yamada WM (2002) Tuning and timing in the gerbil ear: Wiener-kernel analysis. Hear Res 174:206–221

Lin T, Guinan JJ Jr (2004) Time-frequency analysis of auditory-nerve-fiber and basilar-membrane click responses reveal glide irregularities and non-characteristic-frequency skirts. J Acoust Soc Am 116:405–416

Manley GA, Gleich O, Leppelsack HJ, Oeckinghaus H (1985) Activity patterns of cochlear ganglion neurones in the starling. J Comp Physiol A Neuroethol Sens Neural Behav Physiol 157:161–181

Manley GA, Köppl C (1998) Phylogenetic development of the cochlea and its innervation. Curr Opin Neurobiol 8:468–474

Mc Laughlin M, Van de Sande B, van der Heijden M, Joris PX (2007) Comparison of bandwidths in the inferior colliculus and the auditory nerve. I. Measurement using a spectrally manipulated stimulus. J Neurophysiol 98:2566–2579. doi:10.1152/jn.00595.2007

Michelet P, Kovačić D, Joris PX (2012) Ongoing temporal coding of a stochastic stimulus as a function of intensity: time-intensity trading. J Neurosci 32:9517–9527. doi:10.1523/JNEUROSCI.0103-12.2012

Moller AR (1977) Frequency selectivity of single auditory-nerve fibers in response to broadband noise stimuli. J Acoust Soc Am 62:135–142. doi:10.1121/1.381495

Palmer A, Shackleton T (2009) Variation in the phase of response to lowfrequency pure tones in the guinea pig auditory nerve as functions of stimulus level and frequency. J Assoc Res Otolaryngol 10:233–250

Papoulis A (1977) Signal analysis. McGraw-Hill

Peña JL, Viete S, Albeck Y, Konishi M (1996) Tolerance to sound intensity of binaural coincidence detection in the nucleus laminaris of the owl. J Neurosci 16:7046–7054

Recio A, Rhode WS (2000) Basilar membrane responses to broadband stimuli. J Acoust Soc Am 108:2281–2298

Recio A, Rich NC, Narayan SS, Ruggero MA (1998) Basilar-membrane responses to clicks at the base of the chinchilla cochlea. J Acoust Soc Am 103:1972–1989

Recio-Spinoso A, Temchin AN, van Dijk P et al (2005) Wiener-kernel analysis of responses to noise of chinchilla auditory-nerve fibers. J Neurophysiol 93:3615–3634. doi:10.1152/jn.00882.2004

Recio-Spinoso A, Narayan S, Ruggero M (2009) Basilar membrane responses to noise at a basal site of the chinchilla cochlea: quasi-linear filtering. J Assoc Res Otolaryngol 10:471–484. doi:10.1007/s10162-009-0172-0

Rhode WS, Smith PH (1985) Characteristics of tone-pip response patterns in relationship to spontaneous rate in cat auditory nerve fibers. Hear Res 18:159–168. doi:10.1016/0378-5955(85)90008-5

Rossant C, Fontaine B, Goodman DFM (2013) Playdoh: a lightweight python library for distributed computing and optimisation. J Comput Sci 4:352–359. doi:10.1016/j.jocs.2011.06.002

Ruggero MA, Temchin AN (2007) Similarity of traveling-wave delays in the hearing organs of humans and other tetrapods. J Assoc Res Otolaryngol 8:153–166. doi:10.1007/s10162-007-0081-z

Schwartz O, Pillow JW, Rust NC, Simoncelli EP (2006) Spike-triggered neural characterization. J Vis. doi:10.1167/6.4.13

Shera CA (2001) Frequency glides in click responses of the basilar membrane and auditory nerve: their scaling behavior and origin in traveling-wave dispersion. J Acoust Soc Am 109:2023–2034

Shera CA, Guinan JJ Jr (2003) Stimulus-frequency-emission group delay: a test of coherent reflection filtering and a window on cochlear tuning. J Acoust Soc Am 113:2762–2772

Tan Q, Carney LH (2003) A phenomenological model for the responses of auditory-nerve fibers. II. Nonlinear tuning with a frequency glide. J Acoust Soc Am 114:2007

Tan X, Beurg M, Hackney C et al (2013) Electrical tuning and transduction in short hair cells of the chicken auditory papilla. J Neurophysiol 109:2007–2020. doi:10.1152/jn.01028.2012

Temchin AN, Recio-Spinoso A, van Dijk P, Ruggero MA (2005) Wiener kernels of chinchilla auditory-nerve fibers: verification using responses to tones, clicks, and noise and comparison with basilar-membrane vibrations. J Neurophysiol 93:3635–3648. doi:10.1152/jn.00885.2004

Temchin AN, Recio-Spinoso A, Ruggero MA (2011) Timing of cochlear responses inferred from frequency-threshold tuning curves of auditory-nerve fibers. Hear Res 272:178–186. doi:10.1016/j.heares.2010.10.002

Van der Heijden M, Joris PX (2003) Cochlear phase and amplitude retrieved from the auditory nerve at arbitrary frequencies. J Neurosci 23:9194–9198

Van der Heijden M, Joris PX (2006) Panoramic measurements of the apex of the cochlea. J Neurosci 26:11462–11473. doi:10.1523/JNEUROSCI.1882-06.2006

Versteegh CPC, Meenderink SWF, van der Heijden M (2011) Response characteristics in the apex of the gerbil cochlea studied through auditory nerve recordings. J Assoc Res Otolaryngol 12:301–316. doi:10.1007/s10162-010-0255-y

Viete S, Peña JL, Konishi M (1997) Effects of interaural intensity difference on the processing of interaural time difference in the owl's nucleus laminaris. J Neurosci 17:1815–1824

Wagner H (2005) Microsecond precision of phase delay in the auditory system of the barn owl. J Neurophysiol 94:1655–1658. doi:10.1152/jn.01226.2004

Wagner H, Brill S, Kempter R, Carr CE (2009) Auditory responses in the barn owl's nucleus laminaris to clicks: impulse response and signal analysis of neurophonic potential. J Neurophysiol 102:1227–1240. doi:10.1152/jn.00092.2009